



OPEN

SUBJECT AREAS:

COMPOSITES

METHODOLOGY

SOLID-STATE CHEMISTRY

SYNTHESIS AND PROCESSING

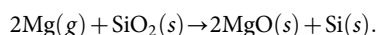
Efficient Fabrication of Nanoporous Si and Si/Ge Enabled by a Heat Scavenger in Magnesiothermic Reactions

Wei Luo¹, Xingfeng Wang¹, Colin Meyers², Nick Wannemacher², Weekit Sirisaksoontorn¹, Michael M. Lerner¹ & Xiulei Ji¹¹Department of Chemistry, ²Department of Chemical Engineering, Oregon State University, Corvallis, Oregon 97331, USA.Received
20 March 2013Accepted
2 July 2013Published
17 July 2013Correspondence and
requests for materials
should be addressed to
X.J. (David.Ji@
oregonstate.edu)

Magnesiothermic reduction can directly convert SiO₂ into Si nanostructures. Despite intense efforts, efficient fabrication of highly nanoporous silicon by Mg still remains a significant challenge due to the exothermic reaction nature. By employing table salt (NaCl) as a heat scavenger for the magnesiothermic reduction, we demonstrate an effective route to convert diatom (SiO₂) and SiO₂/GeO₂ into nanoporous Si and Si/Ge composite, respectively. Fusion of NaCl during the reaction consumes a large amount of heat that otherwise collapses the nano-porosity of products and agglomerates silicon domains into large crystals. Our methodology is potentially competitive for a practical production of nanoporous Si-based materials.

Silicon, the second most abundant element in Earth's crust, has completely changed our way of life by its various applications, particularly in electronics¹. Recently, silicon nanostructures have attracted tremendous attention owing to their potential applications, including photonics, biological imaging, sensors, drug delivery and energy storage^{2–8}. Pure silicon does not exist in nature, but is compounded in silica or silicates. In industry, carbothermal reduction reactions are conducted to produce metallurgical grade silicon (purity > 95%) from silica⁹. However, this approach is unsuitable to synthesize silicon nanostructures due to the high processing temperatures (above 1700 °C). Vapor-liquid-solid (VLS) growth or wafer etching is employed to fabricate silicon nanowires, or nanoporous silicon, respectively^{10,11}. Recently, there have been a few successful syntheses of silicon nanostructures by a molten-salt electrolysis route^{12–14}. A rapid solid-state metathesis was also successfully used to prepare nanostructured silicon¹⁵.

Since Sandhage *et al.* used hot Mg vapor to reduce diatom frustules to porous silicon replicas in 2007¹⁶, various silicon nanostructures, including nanoporous film¹⁷, nanocrystals¹⁸, porous silicon¹⁹, and 1D nanostructures^{20–22} have been synthesized by the same magnesiothermic reduction reaction (MRR):



In these reports, as a general preparation procedure, magnesium powder is located by a certain distance from silica precursors in a reactor. However, the vapor-transport reaction inevitably suffers from reaction inhomogeneity. In a typical product, there are three zones comprising Mg₂Si, Si and unreacted SiO₂, consecutively. In order to improve the reaction homogeneity and yield, magnesium powder and silica were well-mixed and heated in a MRR²³. Nevertheless, the massive heat release from the exothermic reaction (for Mg (g), ΔH = −586.7 kJ/mol_{silica}, or 9.8 kJ/g_{silica})²⁴ collapses the architectures of silica precursors and agglomerates as-synthesized silicon domains into large crystals. More recently, Liu *et al.* succeeded in preparing Si nanocrystals by a MRR in eutectic molten salts as a reaction “solvent”²⁵. Nevertheless, little attention was paid to the exothermic nature of MRR that causes a higher reaction temperature than the set temperature. The heat capacity of molten salts is too low to effectively consume the generated heat. It is reasonable to believe that the reaction temperature would rise by a few hundred degrees. A modest porosity of the Si products (~120 m²/g, and ~0.2 cm³/g) indicates the limitation of the molten-salt route. Thus, it is highly desirable to control the temperature in an exothermic reaction of MRR with an efficient but cost-effective method.

Herein, we report a new preparation strategy for nanoporous Si by using a heat scavenger (NaCl) in a MRR. Fusion of NaCl (ΔH_{fusion} = ~ 28.8 kJ/mol)²⁶ scavenges the heat released in the exothermic reaction, which effectively prevents the structure collapsing and aggregation of the silicon domains. With its low cost and good recyclability, NaCl is a very attractive option. We believe that our new protocol is innovative and effective in



preparing nanoporous silicon. Encouragingly, a nanoporous Si/Ge composite was also successfully fabricated by the same synthetic procedure.

Results

Diatomaceous earth was selected for reduction to its silicon analogue owing to its fine structure and low cost¹⁶. In order to achieve a good mixing level with NaCl, diatom powder was dispersed to an aqueous NaCl solution under stirring at room temperature. The evacuated diatom/NaCl mixture and Mg powder (silica/Mg 1:0.9 in mass) were ground together in an argon-filled glovebox. The reaction mixture was loaded into a Swagelok® reactor (Supplementary Fig. S1) before heating in a tube furnace at 650°C for 2.5 h under Ar. The Si product (referred to as Nano-Si) was collected after NaCl, MgO and residual SiO₂ were removed, consecutively (see Methods). As Energy-Dispersive X-ray (EDX) analysis shows, silicon with nearly the absence of oxides was obtained in Nano-Si (Supplementary Fig. S2a), which is also confirmed by the X-ray photoelectron spectroscopy (XPS) measurement (Supplementary Fig. S2b). The strong peak at 99.3 eV is assigned to the elemental Si, while the much weaker peak around 102.0 eV suggests very little surface oxidation of the Nano-Si. The yield of our preparation is approximately 60%. This is comparable to the solid state metathesis¹⁵. With a larger reactor, porous silicon can be produced at a rate of 560 mg/h

(Supplementary Fig. S3). In a control experiment, a silicon material (designated as Bulk-Si) was prepared by almost the same procedure but without the addition of NaCl.

The synthesized Nano-Si and Bulk-Si were firstly characterized by X-ray diffraction measurements (XRD). As shown in Figure 1a, the XRD peaks exhibited by the two samples can be readily indexed to a cubic phase of silicon (JCPDS No. 27-1402). Compared with the XRD pattern of Nano-Si, the diffraction peaks from Bulk-Si are much narrower, indicative of a much higher degree of crystallinity. The domain size of the Nano-Si is estimated to be 12 nm by the Scherrer Equation based on the (111) peak at 2θ of 28.4°. The domain size of Bulk-Si is clearly much larger than that of Nano-Si, indicated by the sharp XRD peaks. The smaller domain size of Nano-Si can only be attributed to the heat-scavenging effect of NaCl in a MRR. In order to further examine the characteristics of the obtained Si materials, Raman spectra were recorded. Compared with the Bulk-Si, the Raman peak of Nano-Si is slightly broader and shifts towards a lower wavenumber (Fig. 1b). According to the previously reported theoretical fit on porous silicon products, this confirms smaller domain size^{27,28}.

The heat-scavenging effect by the NaCl additive on the morphology of the Si samples can also be seen by Field-Emission Scanning Electron Microscopy (FESEM). Figure 1c and d show the morphology contrast of diatom and Bulk-Si. It is evident that the reaction

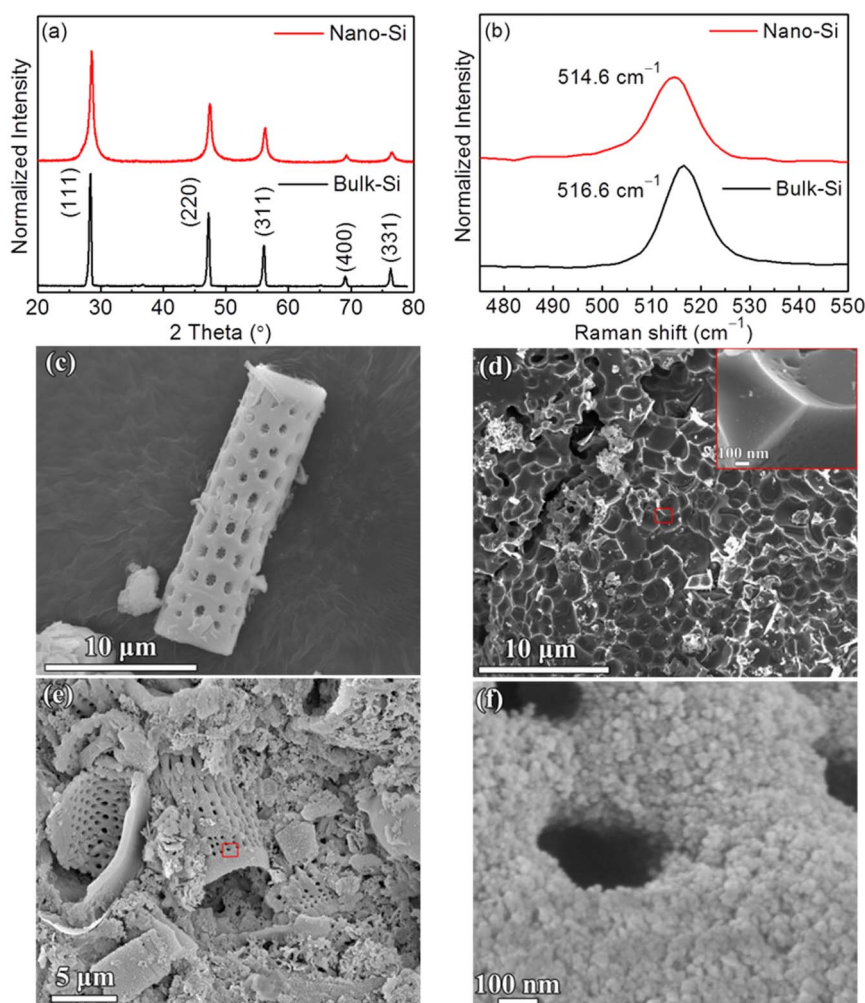


Figure 1 | Structural properties of Nano-Si and Bulk-Si, and morphologies of diatom, Bulk-Si, and Nano-Si, demonstrating the effect of a heat scavenger. (a) XRD patterns and (b) Raman spectra of Nano-Si and Bulk-Si. For an ease of comparison, the XRD and Raman results are normalized to the intensity of the strongest peak. FESEM images of (c) diatom, (d) Bulk-Si and (e) Nano-Si. Inset of (d) is the enlarged FESEM image of Bulk-Si corresponding to the red-square marked area in (d). (f) the enlarged FESEM image of Nano-Si corresponding to the red-square marked area in (e).

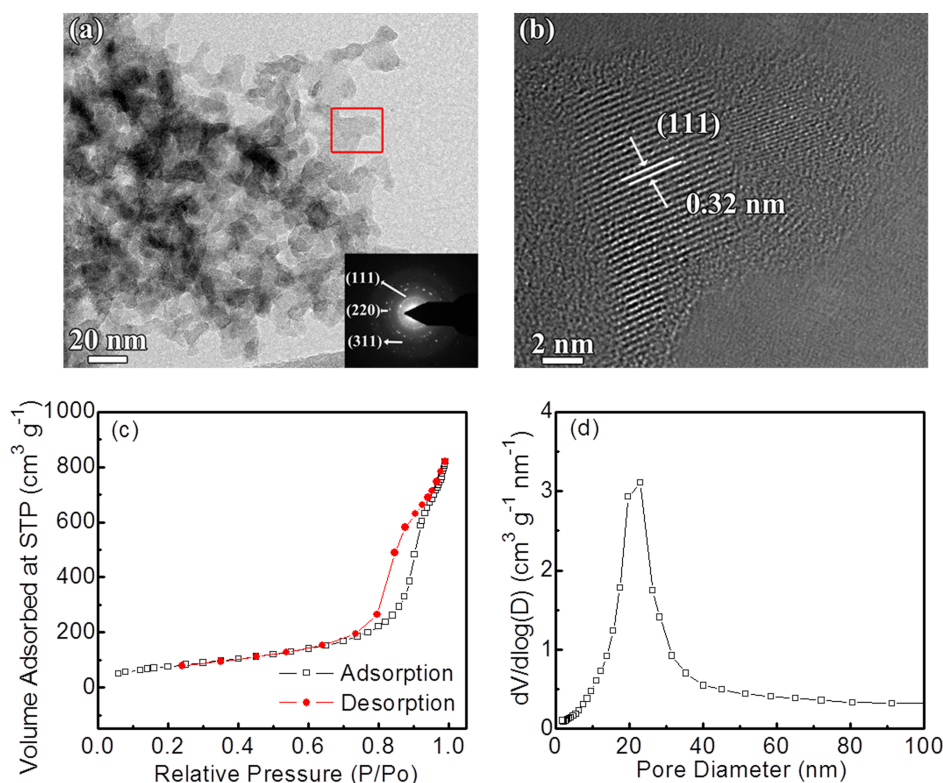


Figure 2 | Microscopy studies, and adsorption/desorption isotherms and pore size distribution analyses of Nano-Si, revealing small domain sizes and high porosity. (a) A TEM image and the corresponding SAED pattern (inset); (b) An HRTEM image that corresponds to the red-square marked area in (a); (c) Nitrogen adsorption-desorption isotherms and (d) pore size distribution of Nano-Si.

completely collapses the original architecture of diatom. Bulk-Si exhibits very smooth surface over a scale of $\sim 1 \mu\text{m}$ (Fig. 1d, inset), suggestive of the formation of large Si crystals. This is consistent to the previous reports on Si products obtained from a MRR with a direct mixing of Mg and silica^{23,29,30}. The dramatic morphological change after the MRR suggests a much higher local reaction temperature than the set temperature of 650°C . It was reported that the measured temperature in a MRR could reach 1720°C ³¹. In contrast to Bulk-Si, with the introduction of NaCl, the cylindrical architectural features of diatom particles were partially maintained in Nano-Si (Fig. 1e). More importantly, Nano-Si has a very rough surface that is composed of ultrafine Si nanocrystals of $\sim 10 \text{ nm}$ in size (Fig. 1f) indicating a relatively low local reaction temperature during the MRR with NaCl involved.

The Transmission Electron Microscopy (TEM) and High-Resolution TEM (HRTEM) images provide more detailed structural information for Nano-Si. As a representative TEM image shows (Fig. 2a), Nano-Si exhibits a nanoporous structure formed by Si nanocrystals about 10 nm in size, consistent with the XRD results. The corresponding selected-area electron diffraction (SAED) pattern reveals diffraction rings of Nano-Si (inset of Fig. 2a), which is consistent with the XRD and Raman results. A representative HRTEM image shows lattice fringes with a d-spacing of 0.32 nm (Fig. 2b) that is assigned to the (111) planes of cubic Si phase. In order to examine the porosity of Nano-Si, nitrogen adsorption and desorption isotherms were measured (Fig. 2c). Calculations based on the isotherms give a Brunauer-Emmett-Teller (BET) surface area of $\sim 295.5 \text{ m}^2/\text{g}$ and a pore volume of $\sim 1.2 \text{ cm}^3/\text{g}$. According to the BET surface area and assuming a density of $2.33 \text{ g}/\text{cm}^3$ of Si, a particle size of $\sim 9 \text{ nm}$ can be estimated for the Nano-Si, which is consistent with the FESEM results (detailed calculation in Supplementary Methods). The pore size distribution shown in Figure 2d suggests that the Nano-Si has pores of about 22 nm in diameter. In contrast,

Bulk-Si exhibits a much lower BET surface area of $\sim 5.2 \text{ m}^2/\text{g}$ and a tiny pore volume of $0.01 \text{ cm}^3/\text{g}$ (Supplementary Fig. S4), indicative of a very dense material.

Besides nanoporous Si, we have further utilized the same synthetic procedure to fabricate a nanoporous Si/Ge composite that may have wide applications in semiconductors³², thermoelectrics^{33,34}, as well as electrochemical energy devices^{35–37}. A composite of Si/Ge oxides were first prepared by a reported sol-gel method with modification (molar ratio between Si and Ge: 9/1)³⁸. The nanoparticle morphology of the Si/Ge oxide composite is shown in Figure 3a. The particle size is around 30 nm , as shown in a TEM image (Supplementary Fig. S5a). A high angle annular dark field scanning TEM (HAADF-STEM) image and the corresponding Si and Ge EDX mappings reveal that GeO_2 particles are encapsulated in the matrix of SiO_2 larger particles with a clear contrast (Supplementary Fig. S5b). The brighter parts match the Ge EDX mapping. MRRs were conducted for Si/Ge oxides with and without NaCl additive at 650°C for 2.5 h under Ar. Without NaCl additive, a Si/Ge product collected after a similar procedure for diatom (designated as Bulk-SiGe) comprises large agglomerates with macropores, as a representative SEM image shows (Fig. 3b). On the other hand, with NaCl, the nanoparticle morphology of Si/Ge oxides has been well-maintained after the MRR, as shown by the FESEM images (Fig. 3c and d). It is evident that the Si/Ge composite (referred to as Nano-SiGe) is composed of nanoparticles sized around 10 nm . EDX analysis also verifies that little oxides exist in the final Nano-SiGe products (Supplementary Fig. S6).

The crystalline phases of the Si/Ge composites were investigated by XRD. As Figure 4a shows, the XRD pattern of Bulk-SiGe displays the cubic phase similar to that of Bulk-Si. The Ge phase reflections are invisible in the XRD pattern, indicating the formation of a solid solution of Ge in the matrix of cubic silicon phase. In sharp contrast, the XRD pattern of Nano-SiGe clearly reveals both elemental phases

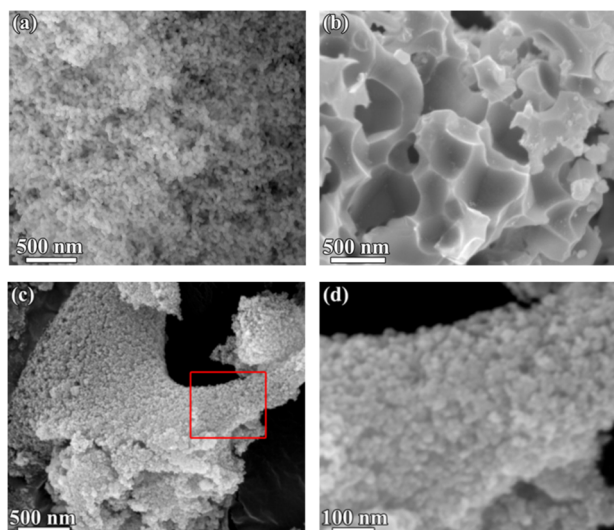


Figure 3 | FESEM images showing morphologies of Si/Ge oxides, Nano-SiGe and Bulk-SiGe. (a) SiGe oxides; (b) Bulk-SiGe; (c) Nano-SiGe; (d) An enlarged FESEM image of Nano-SiGe corresponding to the red-square marked area in (c).

of Si and Ge (Fig. 4b). Five pairs of peaks in the vicinity of 28° , 47° , 55° , 68° , and 75° are ascribed to the reflections of (111), (220), (311), (400), and (331) planes of Ge or Si, respectively. These peaks can be deconvoluted into the components from elemental Si and Ge cubic phases (Fig. 4c and Supplementary Fig. S7). The domain size is ~ 20 nm for Ge and ~ 6 nm for Si, estimated by the Scherrer Equation on the (111) peaks. A smaller silicon domain size in Nano-SiGe than that of Nano-Si can be attributed to a more efficient heat-scavenging effect due to the higher specific pore volume of SiGe oxides ($0.41 \text{ cm}^3/\text{g}$) than diatom ($0.056 \text{ cm}^3/\text{g}$) (Supplementary Fig. S8). In the Raman spectra of Nano-SiGe, the peaks at 509.8 , 404.7 , and 294.8 cm^{-1} from elemental Si, SiGe alloy, and elemental Ge, respectively, are observed while only a peak of Si at 513.0 cm^{-1} shows up in Bulk-SiGe (Fig. 4d). The surface oxidation states and the chemical composition of the Nano-SiGe were further examined by XPS. Similar to Nano-Si, the peak at 99.3 eV in the Nano-SiGe is contributed by elemental Si [2p] (Fig. 4e). Moreover, the peak at 29.4 eV can be ascribed to elemental Ge [3d] (Fig. 4f). Owing to slight surface oxidation, a weak peak around 32.0 eV is also detected. Judging from Raman spectra peak intensities and combining the XRD and XPS results, it can be concluded that the elemental phase is the primary phase for Ge element.

TEM and HRTEM were carried out to further study the microstructure of Nano-SiGe. As shown in Figure 5a,d, Nano-SiGe consists of nanocrystals and a large number of nanosized pores. The

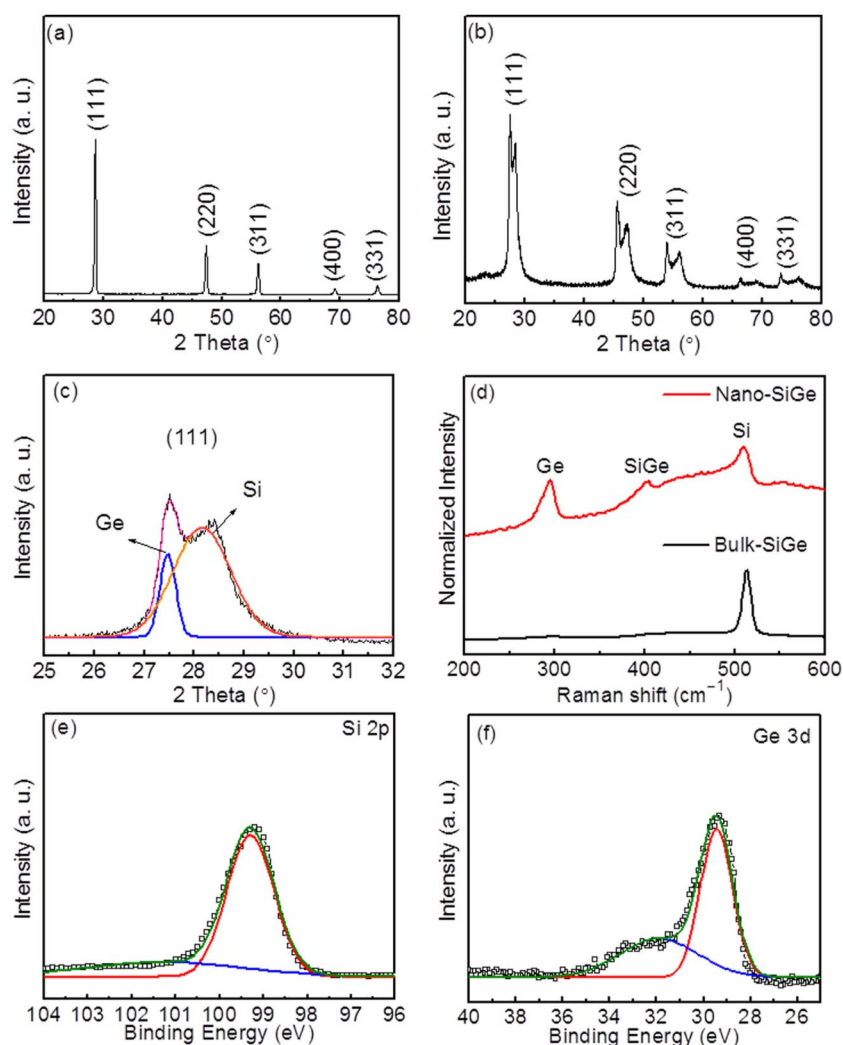


Figure 4 | Structural information of Si/Ge products via XRD and Raman, showing the sharp contrast between Bulk-SiGe and Nano-SiGe. XRD patterns of (a) Bulk-SiGe and (b) Nano-SiGe; (c) XRD of the (111) peaks for the Nano-SiGe. (d) Raman spectra of Bulk-SiGe and Nano-SiGe. XPS spectra of Nano-SiGe showing signals of (e) Si [2P] and (f) Ge [3d].

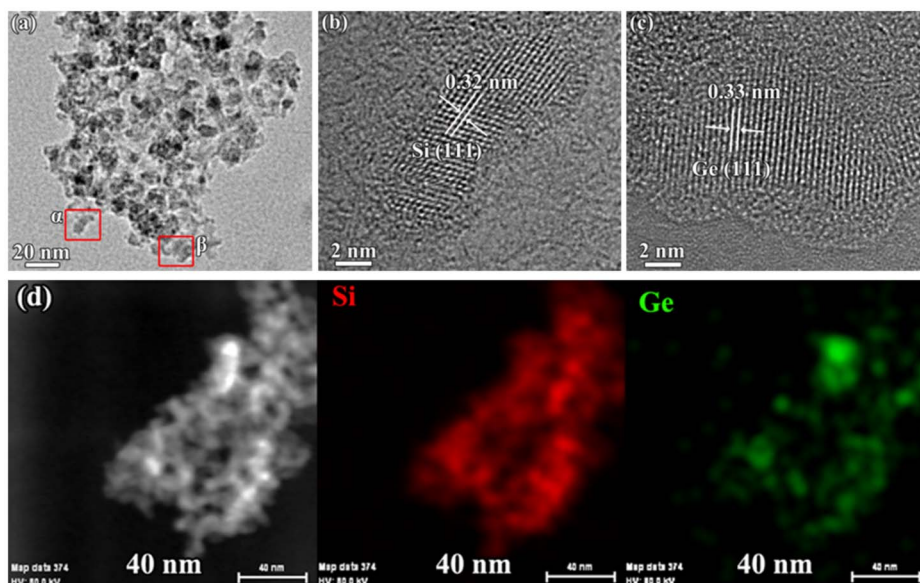


Figure 5 | Microstructural information and chemical composition of Nano-SiGe. TEM images of the Nano-SiGe, (a) at low magnification; (b, c) HRTEM that correspond to the areas in (a) are marked by the red-squares α and β , respectively; (d) HADDF-STEM and EDX elemental mapping images of Nano-SiGe.

HRTEM images in Figure 5b and c display two types of lattice fringes with spacings of 0.32 nm and 0.33 nm, respectively. These may correspond to the (111) planes of Si and Ge, respectively. We further investigated the homogeneity of Si and Ge particles in the Nano-SiGe product (Fig. 5d). HAADF-STEM does not show much contrast between Si and Ge, unlike GeO_2 and SiO_2 . From the EDX mappings, it is evident that both Si and Ge are nearly homogeneously distributed in the Nano-SiGe composite. The BET surface area of Nano-SiGe is $180.4 \text{ m}^2/\text{g}$ with a pore volume of $0.73 \text{ cm}^3/\text{g}$. These characteristics are smaller than Nano-Si although a more porous precursor was used. In contrast, Bulk-SiGe only exhibits a BET surface area of $4.9 \text{ m}^2/\text{g}$ and a pore volume of $0.015 \text{ cm}^3/\text{g}$ (see isotherms in Supplementary Fig. S9). To the best of our knowledge, this is the first time that porous Si/Ge nanocomposite with Ge primarily in its elemental phase has been synthesized by a simple MRR. This method may pave the way to the efficient production of porous Si/Ge nanostructures. Important applications may take advantage of the unique properties of the new Si/Ge nanostructure.

Discussion

We propose the following process for the MRR with the NaCl heat scavenger. When the furnace temperature rises close to the melting point of Mg at 650°C , the exothermic MRR is initiated. Without an efficient dissipation, heat released by the reaction accumulates, and the reaction temperature continues to rise. At 801°C , NaCl in the reaction mixture begins to melt, which consumes the heat generated by the MRR and retards further temperature rising. For one gram of silica, we used 10 grams of NaCl heat scavenger. It takes approximately 1.4 kJ to heat up the reaction mixture from 650°C to 801°C . With good thermal conductivity of molten NaCl ($0.8 \text{ W/m}\cdot\text{K}$)³⁹, heat from the MRR can be readily conducted to surrounding NaCl crystals and consumed by NaCl fusion. The fusion of NaCl (10 g) removes heat of 5.0 kJ . At 801°C , in fact, Mg vaporization heat should be partially provided by the MRR as well (Mg: $\Delta H_{\text{vap}} = 6.1 \text{ kJ/g}$). Totally, the heat consumption by the reactant mixture is between 6.4 kJ to 12.5 kJ , comparable to the heat release from the MRR ($9.8 \text{ kJ/g}_{\text{silica}}$). We can expect that the reaction temperature may be slightly higher than 801°C . In order to probe the real reaction temperatures, we used alkaline carbonates as temperature indicators that were well mixed with the reactants (Supplementary Methods).

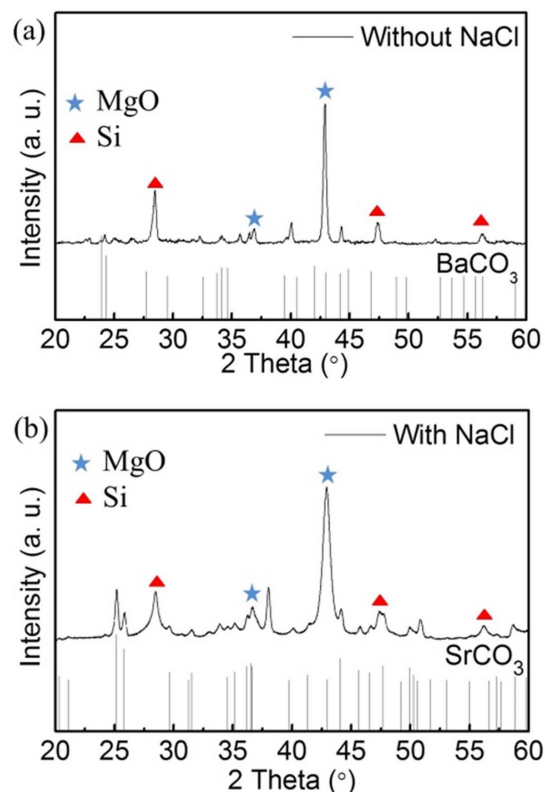


Figure 6 | Investigation of decomposition of alkaline carbonates during a MRR without or with NaCl heat scavenger, indicating a much lower reaction temperature with the heat scavenger. XRD patterns of (a) the product collected after heating the mixture of diatom, Mg powder, and BaCO_3 at 650°C for 2.5 h under Ar and (b) the product collected after heating the mixture of diatom, Mg powder, NaCl, and SrCO_3 at 650°C for 2.5 h under Ar and the removal of NaCl.



After a MRR without NaCl, the absence of BaCO₃ peaks in the XRD pattern of the product indicates a reaction temperature above 1300 °C, the decomposition temperature of BaCO₃ (Fig. 6a), consistent to the reported reaction temperature³¹. In sharp contrast, with NaCl heat scavenger, SrCO₃, with the decomposition temperature of 1100 °C, survives a MRR in the product, confirmed by its strong XRD peaks and a lack of XRD peaks from other Sr containing compounds than SrCO₃ (Fig. 6b). However, XRD peaks of CaCO₃ disappeared after a MRR even with NaCl as the heat scavenger (see XRD results in Supplementary Fig. S10). Even with 20 g NaCl that is theoretically sufficient to absorb all the heat, CaCO₃ still decomposes. This implies that the method could be limited by the mixing degree between NaCl and diatom. We are currently working on porous silica nanofibers as precursors in order to increase the mixing extent with NaCl heat scavenger. The results reveal that the reaction temperature with NaCl should be between 840 °C and 1100 °C. This is the first time that the real reaction temperature in a magnesiothermic reaction can be controlled by a heat scavenger and “measured” with a temperature indicator.

In summary, we present here a new preparation strategy that employs a heat scavenger (NaCl) to fabricate the nanoporous silicon-based materials by heating the mixture of silica precursors, Mg powder and NaCl, a highly effective reaction setup. Fusion of NaCl effectively scavenges much heat released in the exothermic MRR, which minimizes the pore-structure collapse of the product and aggregation of nano-domains. Nanoporous Si was obtained from diatoms with a high yield. A porous Si/Ge nanocomposite with Ge primarily in its elemental phase has been synthesized by a simple MRR for the first time. By using alkaline carbonates as temperature indicators, we measured the real reaction temperature in MRRs that is between 840 °C to 1100 °C at the presence of NaCl. We believe this new strategy can be regarded as a general synthetic method for different types of nanosized materials synthesized by highly exothermic reactions.

Methods

Synthesis of Nano-Si. Nanoporous silicon was prepared *via* a modified magnesiothermic reduction reaction. Diatom was dispersed to an aqueous NaCl solution under stirring at room temperature (Silica/NaCl: 1/10 in weight). The mixture was heated to 60 °C under vigorous stirring followed by drying under vacuum at 150 °C to remove water. Dried diatom/NaCl powder (11 g) and 0.9 g Mg powder was ground together under an Ar atmosphere and then sealed in a Swagelok® reactor. Then, the diatom/NaCl/Mg mixture was heated in a tube furnace at 650 °C for 2.5 h under an Ar atmosphere. After cooling to room temperature, the obtained products were first immersed in a H₂O/EtOH solution, where NaCl can be recycled by drying the filtrate. Then, 1 M HCl and 5% aqueous HF were used to remove MgO and surface-grown SiO₂, respectively. Finally, the nanoporous silicon products were collected, washed with EtOH, and vacuum-dried at 60 °C overnight.

Synthesis of Nano-SiGe. Nano-sized SiGe oxides were first prepared by a reported sol-gel method with slight modification. In a typical synthesis, tetraethyl orthosilicate (0.75 g) and germanium ethoxide (0.1 g) was mixed with ethanol (28 ml) by sonication for 10 minutes. Then, a mixture of DI water (5.6 mL) and ammonium hydroxide (0.84 mL) was added into the above Si/Ge/ethanol solution under stirring at room temperature. This mixture was stirred for 24 h and the obtained white precipitate was centrifuged, washed and dried. The sample was then heated in a muffle furnace at 500 °C for 4 h in air to remove remaining organic impurities. Then, the SiGe oxides were treated as described above to fabricate the Bulk-SiGe and the Nano-SiGe products.

Characterization. X-Ray diffraction (XRD) patterns were collected using a Rigaku Ultima IV Diffractometer with Cu K α irradiation ($\lambda = 1.5406 \text{ \AA}$). Raman spectra were recorded with a DXR SmartRaman Spectrometer (Thermo Scientific) using a Diode laser at 780 nm. For ease of comparison, the XRD and Raman results are normalized to the intensity of the strongest peak. X-ray photoelectron spectroscopy (XPS) measurements were carried out on an ESCALAB 250 X-ray Photoelectron Spectrometer (ThermoScientific). The morphology was examined by field emission scanning electron microscopy (FESEM) using an FEI NOVA 230 high resolution SEM with an energy-dispersive X-ray (EDX) attachment. Transmission electron microscopy (TEM) and high-resolution transmission electron microscopy (HRTEM) images were recorded by an FEI Titan 80–300 TEM. High angle annular dark field scanning TEM (HAADF-STEM) measurements were carried out on an FEI Titan 80–200 microscope coupled with a HAADF detector and an EDX spectrometer.

Nitrogen sorption measurements were performed on a Micromeritics ASAP 2020 analyzer and a TriStar II 3020 analyzer.

- Cui, Y. & Lieber, C. M. Functional nanoscale electronic devices assembled using silicon nanowire building blocks. *Science* **291**, 851–853 (2001).
- Liu, A. *et al.* A high-speed silicon optical modulator based on a metal–oxide–semiconductor capacitor. *Nature* **427**, 615–618 (2004).
- Henderson, E. J. *et al.* Colloidally stable silicon nanocrystals with near-infrared photoluminescence for biological fluorescence imaging. *Small* **7**, 2507–2516 (2011).
- Baratto, C. *et al.* Front-side micromachined porous silicon nitrogen dioxide gas sensor. *Thin Solid Films* **391**, 261–264 (2001).
- Li, Y. Y. *et al.* Polymer replicas of photonic porous silicon for sensing and drug delivery applications. *Science* **299**, 2045–2047 (2003).
- Cui, L. F., Ruffo, R., Chan, C. K., Peng, H. & Cui, Y. Crystalline-amorphous core–shell silicon nanowires for high capacity and high current battery electrodes. *Nano Lett.* **9**, 491–495 (2009).
- Chan, C. K. *et al.* High-performance lithium battery anodes using silicon nanowires. *Nat. Nanotechnol.* **3**, 31–35 (2008).
- Chen, D. *et al.* Reversible lithium-ion storage in silver-treated nanoscale hollow porous silicon particles. *Angew. Chem. Int. Ed.* **51**, 2409–2413 (2012).
- Nagamori, M., Malinsky, I. & Claveau, A. Thermodynamics of the Si–C–O system for the production of silicon carbide and metallic silicon. *Metall. Trans. B* **17**, 503–514 (1986).
- Morales, A. M. & Lieber, C. M. A laser ablation method for the synthesis of crystalline semiconductor nanowires. *Science* **279**, 208–211 (1998).
- Cunin, F. *et al.* Biomolecular screening with encoded porous-silicon photonic crystals. *Nat. Mater.* **1**, 39–41 (2002).
- Nohira, T., Yasuda, K. & Ito, Y. Pinpoint and bulk electrochemical reduction of insulating silicon dioxide to silicon. *Nat. Mater.* **2**, 397–401 (2003).
- Jin, X., Gao, P., Wang, D., Hu, X. & Chen, G. Z. Electrochemical preparation of silicon and its alloys from solid oxides in molten calcium chloride. *Angew. Chem. Int. Ed.* **43**, 733–736 (2004).
- Cho, S. K., Fan, F.-R. F. & Bard, A. J. Electrodeposition of crystalline and photoactive silicon directly from silicon dioxide nanoparticles in molten CaCl₂. *Angew. Chem. Int. Ed.* **51**, 12740–12744 (2012).
- Bux, S. K. *et al.* Rapid solid-state synthesis of nanostructured silicon. *Chem. Mater.* **22**, 2534–2540 (2010).
- Bao, Z. *et al.* Chemical reduction of three-dimensional silica micro-assemblies into microporous silicon replicas. *Nature* **446**, 172–175 (2007).
- Richman, E. K., Kang, C. B., Brezesinski, T. & Tolbert, S. H. Ordered mesoporous silicon through magnesium reduction of polymer templated silica thin films. *Nano Lett.* **8**, 3075–3079 (2008).
- Gallego-Gomez, F. *et al.* Light emission from nanocrystalline Si inverse opals and controlled passivation by atomic layer deposited Al₂O₃. *Adv. Mater.* **23**, 5219–5223 (2011).
- Khripin, C. Y., Pristinski, D., Dunphy, D. R., Brinker, C. J. & Kaehr, B. Protein-directed assembly of arbitrary three-dimensional nanoporous silica architectures. *ACS Nano* **5**, 1401–1409 (2011).
- Zhang, Y. & Huang, J. Hierarchical nanofibrous silicon as replica of natural cellulose substance. *J. Mater. Chem.* **21**, 7161–7165 (2011).
- Yoo, J. K., Kim, J., Jung, Y. S. & Kang, K. Scalable fabrication of silicon nanotubes and their application to energy storage. *Adv. Mater.* **24**, 5452–5456 (2012).
- Tao, H. C., Fan, L. Z. & Qu, X. Facile synthesis of ordered porous Si@C nanorods as anode materials for Li-ion batteries. *Electrochim. Acta* **71**, 194–200 (2012).
- Yu, Y. *et al.* Reversible storage of lithium in silver-coated three-dimensional macroporous silicon. *Adv. Mater.* **22**, 2247–2250 (2010).
- Dean, J. A. *Langer's Handbook of Chemistry*. 15th edn (McGraw-Hill, 1999).
- Liu, X., Giordano, C. & Antonietti, M. A molten-salt route for synthesis of Si and Ge nanoparticles: chemical reduction of oxides by electrons solvated in salt melt. *J. Mater. Chem.* **22**, 5454–5459 (2012).
- Zalba, B., Marín, J. M., Cabeza, L. F. & Mehling, H. Review on thermal energy storage with phase change: materials, heat transfer analysis and applications. *Appl. Therm. Eng.* **23**, 251–283 (2003).
- Xu, D. *et al.* Optical Absorption and Photoluminescence Studies of Free-Standing Porous Silicon Films with High Porosities. *J. Phys. Chem. B* **103**, 5468–5471 (1999).
- Hai, N. H., Grigoriantz, I. & Gedanken, A. Converting stober silica and mediterranean sand to high surface area silicon by a reaction under autogenic pressure at elevated temperatures. *J. Phys. Chem. C* **113**, 10521–10526 (2009).
- Shen, L., Guo, X., Fang, X., Wang, Z. & Chen, L. Magnesiothermally reduced diatomaceous earth as a porous silicon anode material for lithium ion batteries. *J. Power Sources* **213**, 229–232 (2012).
- Wang, M.-S., Fan, L.-Z., Huang, M., Li, J. & Qu, X. Conversion of diatomite to porous Si/C composites as promising anode materials for lithium-ion batteries. *J. Power Sources* **219**, 29–35 (2012).
- Won, C. W., Nersisyan, H. H. & Won, H. I. Solar-grade silicon powder prepared by combining combustion synthesis with hydrometallurgy. *Sol. Energy Mater. Sol. Cells* **95**, 745–750 (2011).



32. Lee, M. L., Fitzgerald, E. A., Bulsara, M. T., Currie, M. T. & Lochtefeld, A. Strained Si, SiGe, and Ge channels for high-mobility metal-oxide-semiconductor field-effect transistors. *J. Appl. Phys.* **97**, 011101–011128 (2005).
33. Joshi, G. *et al.* Enhanced Thermoelectric Figure-of-Merit in Nanostructured p-type Silicon Germanium Bulk Alloys. *Nano Lett.* **8**, 4670–4674 (2008).
34. Mingo, N., Hauser, D., Kobayashi, N. P., Plissonnier, M. & Shakouri, A. “Nanoparticle-in-Alloy” Approach to Efficient Thermoelectrics: Silicides in SiGe. *Nano Lett.* **9**, 711–715 (2009).
35. Song, T. *et al.* Si/Ge Double-Layered Nanotube Array as a Lithium Ion Battery Anode. *ACS Nano* **6**, 303–309 (2012).
36. Hwang, C. M. & Park, J. W. Electrochemical characterizations of multi-layer and composite silicon-germanium anodes for Li-ion batteries using magnetron sputtering. *J. Power Sources* **196**, 6772–6780 (2011).
37. Wang, J. Z., Du, N., Zhang, H., Yu, J. X. & Yang, D. R. Cu-Si1-xGex core shell nanowire arrays as three-dimensional electrodes for high-rate capability lithium-ion batteries. *J. Power Sources* **208**, 434–439 (2012).
38. Strandwitz, N. C. & Stucky, G. D. Hollow Microporous Cerium Oxide Spheres Templated By Colloidal Silica. *Chem. Mater.* **21**, 4577–4582 (2009).
39. Galamba, N., de Castro, C. N. & Ely, J. Thermal conductivity of molten alkali halides from equilibrium molecular dynamics simulations. *J. Chem. Phys.* **120**, 8676–8682 (2004).

Acknowledgments

We thank Oregon State University for the financial supports for this work. We thank Professor May Nyman and Dr. Yu Hou for Raman measurements. We are thankful to

Professor Mas Subramanian, Dr. Lev Zakharov, and Whitney Schmidt for the XRD measurements, and Dr. Stephen Golledge for the XPS measurements. We appreciate the help from Teresa Sawyer, Dr. Peter Eschbach and Joshua Razink for their kind help in TEM measurements in OSU EM Facility, funded by National Science Foundation, Murdock Charitable Trust and Oregon Nanoscience and Microtechnologies Institute, and CAMCOR EM Facility.

Author contributions

W.L. and X.J. designed and conducted the research. W.L., X.F.W. and C.M. prepared the materials. XRD and Raman experiments were performed by W.L. and W.S. and BET measurements were performed by N.W.; X.J., W.L. and M.M.L. wrote the paper. All the authors analyzed and discussed the experimental results.

Additional information

Supplementary information accompanies this paper at <http://www.nature.com/scientificreports>

Competing financial interests: The authors declare no competing financial interests.

How to cite this article: Luo, W. *et al.* Efficient Fabrication of Nanoporous Si and Si/Ge Enabled by a Heat Scavenger in Magnesiothermic Reactions. *Sci. Rep.* **3**, 2222; DOI:10.1038/srep02222 (2013).



This work is licensed under a Creative Commons Attribution-NonCommercial-NoDerivs 3.0 Unported license. To view a copy of this license, visit <http://creativecommons.org/licenses/by-nc-nd/3.0>